
Article:
Dolcetti, G. orcid.org/0000-0002-0992-0319 and García Nava, H. (2019) Wavelet spectral analysis of the free surface of turbulent flows. Journal of Hydraulic Research, 57 (2). pp. 211-226. ISSN 0022-1686

https://doi.org/10.1080/00221686.2018.1478896

To appear in the *Journal of Hydraulic Research*
Vol. 00, No. 00, Month 20XX, 1–22

Research paper

Wavelet spectral analysis of the free surface of turbulent flows

GIULIO DOLCETTI (IAHR Member), Research Associate, *Department of Mechanical Engineering, The University of Sheffield, Sheffield, United Kingdom*
Email: g.dolcetti@sheffield.ac.uk (author for correspondence)

HÉCTOR GARCÍA NAVA, Research Scientist, *Instituto de Investigaciones Oceanológicas, Universidad Autónoma de Baja California, Ensenada, México*
Email: hector.gnava@uabc.edu.mx

Running Head: Wavelet spectral analysis of turbulent flow surface

February 2018

Wavelet spectral analysis of the free surface of turbulent flows

ABSTRACT
This work demonstrates the applicability of the wavelet directional method as a mean of characterizing the free surface dynamics in shallow turbulent flows using a small number of sensors. The measurements are obtained with three conductance wave probes in a laboratory flume, in a range of subcritical flow conditions where the Froude number was smaller than one, and the bed was homogeneously rough. The characteristic spatial scale of the surface elevation is found to correspond to the wavelength of stationary waves oriented against the flow. The spectrum of the dominant distribution of waves is characterized in terms of an angular spreading function. A new procedure to estimate the mean surface velocity based on measurements of the surface elevation at only two locations is proposed. The results can inform the development of more accurate models of the surface behavior, with applications for the remote sensing of rivers and open channel flows.

Keywords: Air-water interface interactions; gravity waves; hydrodynamic waves; laboratory studies; velocity measurements

1 Introduction

The dynamics of the air-water interface in turbulent open channel water flows have been the subject of a number of experimental (Dolcetti, Horoshenkov, Krynkin, & Tait, 2016; Fujita, Furutani, & Okanishi, 2011; Horoshenkov, Nichols, Tait, & Maximov, 2013; Longo, 2010, 2011; Savelsberg & Van De Water, 2009), theoretical (Longo, Chiapponi, & Liang, 2013; Nichols, Tait, Horoshenkov, & Shepherd, 2016; Teixeira & Belcher, 2006), and numerical (Borue, Orszag, & Staroselsky, 1995; Guo & Shen, 2010) works. The shape and dynamics of the patterns on the rough free surface are of importance for the exchange of gas and momentum across the interface (Tamburrino & Martínez, 2017; Turney & Banerjee, 2013), for the monitoring of riverine habitat (Milan, Heritage, Large, & Entwistle, 2010), and for the accuracy of remote sensing techniques (Dolcetti & Krynkin, 2017; Dolcetti, Krynkin, & Horoshenkov, 2017; Legleiter, Mobley, & Overstreet, 2017).

A strong interaction between turbulence and the free surface has been demonstrated experimentally for supercritical flows with the Froude number $\mathsf{F} > 1$ (e.g., Wang, Felder, & Chanson, 2014; Wang, Murzyn, & Chanson, 2015), or for turbulence that is generated behind a Crump weir (Longo, 2010, 2011) or a grid (Savelsberg & Van De Water, 2009), also in still water (Chiapponi, Longo, & Tonelli, 2012). The focus of the present work is on the subcritical flows where turbulence originates due to the presence of a boundary layer near a rough bed, and where the depth is not too large so that the effects of the bed roughness on the free surface are not negligible. In these conditions, which are believed to be of importance for geophysical and industrial flows, most studies suggest that the surface patterns are a mixture of gravity-capillary waves and passive localized deformations induced by turbulent pressure fluctuations (Brocchini & Peregrine, 2001), and that the characteristic temporal and spatial scales of the surface deformation are related to the conditions of the turbulent flow. The characteristic surface horizontal scale has been linked to the typical scales of turbulence (Fujita et al., 2011; Horoshenkov et al., 2013; Nichols et al., 2016), but also to the wavelength of the stationary waves with the crests perpendicular to the direction of the mean flow, that originate due to the presence of a rough static bed (Dolcetti et al., 2016).

The relationship between the scales of the flow and those of the free surface potentially allows the remote characterization of the flow conditions, based on the measurements of the water surface elevation. However, these mesaurements are difficult because they require good spatial and temporal resolution over relatively large measurement areas. The existing techniques that are able to characterize the surface elevation are of difficult application in the field (Cobelli, Maurel, Pagneux, & Petitjeans, 2009), or can only measure a spatially limited area of the surface (Krynkin, Horoshenkov, & Van Renterghem, 2016; Nichols, Tait, Horoshenkov, & Shepherd, 2013). The wavelet directional method (WDM) was introduced by Donelan, Drennan, and Magnusson (1996) as an experimental technique to characterize the non-stationary statistics of ocean waves.

The method allows the simultaneous spatial and temporal characterization of the water surface, with a limited number of measurement locations. To the better of our knowledge, the method has never been applied to measurements in open-channel flows, although its validity in weakly non-stationary or non-homogeneous conditions make it particularly suitable for applications where small horizontal velocity gradients or slowly changing conditions are present, and where a Fourier analysis would not be applicable. The technique can be easily applied to remote measurements of the surface made over a limited area.

In this work, the applicability of the WDM as a mean of characterizing the free surface dynamics in shallow turbulent flows with a small number of measurement locations is demonstrated. The WDM is applied to measurements of the free surface elevation obtained in a laboratory flume, in a range of subcritical flow conditions with Froude number $\mathsf{F} = U_0(gd)^{-1/2} < 1$, where U_0 is the mean surface flow velocity, g is the gravity constant, and d is the mean flow depth. The measurements obtained with the WDM using only three conductance wave probes confirm and extend previous results obtained with a two-dimensional Fourier analysis using 16 probes by Dolcetti et al. (2016). The stationary gravity-capillary waves oriented against the flow are found to dominate the surface spectrum, and to represent the characteristic horizontal scales of the surface, whenever the mean surface velocity is larger than the minimum phase speed of gravity-capillary waves. The characteristics of the dominant three-dimensional distribution of waves, suggested by Dolcetti et al. (2016) based on independent measurements in two dimensions, are confirmed and quantified in terms of an angular spreading function. A simplified surface model based on these results is presented, and shown to explain the behavior observed by Horoshenkov et al. (2013). As a proof of the potential of the WDM for monitoring the conditions of turbulent flows, the possibility to estimate the mean surface velocity using only two sensors aligned along the streamwise direction is demonstrated.

This paper is organized as follows. The experimental setup is presented in section 2. The details of the analysis procedure based on the WDM are reported in section 3. In section 4, the fundamental equations that describe the dynamics of gravity-capillary waves in sheared flows are reported. The experimental results are presented in section 5. A technique to estimate the mean surface velocity based on the measured spectra is presented in section 6. The relevance of the results is discussed in section 7. Finally, conclusions are drawn in section 8.

2 Experimental setup

2.1 *Experimental flume*

The experiments were performed in a 12 m long and 0.459 m wide rectangular laboratory flume with homogeneous bed roughness. The bed of the flume was covered with three layers of plastic spheres with the diameter d_s equal to 25.4 mm, arranged according to a hexagonal compact lattice. The flume bed slope and the flow discharge were controlled in order to obtain the desired combination of flow mean depth and velocity. An adjustable gate at the outlet of the flume ensured that the time-averaged flow depth, d, was homogeneous along the flume. This depth was measured with a set of manual depth gauges, with respect to a datum at the distance $d_s/4$ below the crest of the spheres. The uncertainty of these measurements was estimated as ± 0.5 mm. The mean streamwise surface velocity, U_0, was measured by timing the passage of buoyant particles along a streamwise distance of 1.53 m, with the estimated relative uncertainty of 3.5 %. All depth and velocity measurements were averaged over independent consecutive measurements, obtained with the same bed slope and discharge.

Thirteen different flow conditions, identified by the values of d, and U_0, were tested. These are reported in Table 1, together with the Reynolds numbers based on the mean surface velocity and homogeneous mean depth, $\mathsf{R} = U_0 d/\nu$, where ν is the kinematic viscosity of water, and the Froude numbers, $\mathsf{F} = U_0(gd)^{-1/2}$. The other quantities listed in Table 1 correspond to the standard

deviation of the surface elevation, σ_ζ, the value of the characteristic wavelength of the surface waves, $2\pi/k_0$, and the parameter b of the angular spreading function. These last two quantities are introduced with more detail in sections 3 and 4. In condition 1 the mean surface velocity was smaller than the minimum phase speed of gravity-capillary waves in still water. For this flow condition, the patterns on the free surface behave differently due to the absence of stationary waves. Therefore, the analysis for this flow condition is presented separately, and the wavelength $2\pi/k_0$ is not indicated in Table 1.

2.2 *Measurement of the surface elevation*

The surface elevation was measured in time using a set of conductance wave probes. Details of the measurement apparatus and data acquisition system used for this study have been described in section II of the paper by Dolcetti et al. (2016). For this work, three probes, labeled A, B, and C, were installed at the distance of 9 m from the flume inlet in an L-shape arrangement, as shown in Fig. 1. Each probe comprised of two 0.24 mm thick tinned copper wires aligned transversally to the mean flow direction. The wires were anchored to the bottom and pierced the water surface vertically. The spacing between the two wires was 13 mm for probes A and B, and 11 mm for probe C. The probes A and B were aligned along the x-direction, which was parallel to the direction of the mean flow and coincided with the flume centerline. The probes A and C were aligned along the y-direction, which was transverse to the flow direction (see Fig. 1). The co-ordinates of each probe A, B, and C, are written as $\boldsymbol{r}_A = (0, 0)$, $\boldsymbol{r}_B = (L_x, 0)$, and $\boldsymbol{r}_C = (0, L_y)$, respectively, where $L_x = 26$ mm was the distance between probes A and B, and $L_y = 35$ mm was the distance between probes A and C. These distances were chosen as a compromise between the spectral resolution and the accuracy of the WDM.

For each flow conditions, the instantaneous free surface elevation was measured at each wave probe with a sampling frequency of 500 Hz, for a duration of ten minutes. A second-order Butterworth band-pass filter with the cut-off frequencies of 0.1 Hz and 20 Hz was applied to the data to eliminate electric noise at high frequency. After filtering, the data was downsampled to a frequency of 50 Hz, and analyzed with the WDM.

The maximum resolution allowed by the measurements with wave probes depends on the height of the meniscus which forms around the wires (Longo, 2012). Additional uncertainties arise due to cross-talking between different probes. The height of the meniscus was estimated to be comparable to the radius of the probe wires, 0.12 mm. The effects of the filter on the uncertainty of the analysis were tested based on synthetic signals, and were found negligible compared to the other sources of uncertainty. As a further check of the accuracy of the spectral estimates obtained with the wave probes, the frequency spectra of the surface elevation measured with wave probe A and with an ultrasonic sensor positioned at $x = -1$ m were compared. The measurement with the ultrasonic sensor was obtained based on the technique described by Nichols et al. (2013), using a pair of TR-89B Series Type 40 transducers manufactured by Massa Product Corporation operating at 39 kHz. The measurement was performed in flow condition 2, for which the uncertainty of the ultrasonic sensor was estimated to be approximately 10 % of the wave amplitude (Nichols et al., 2013). The difference between the spectra obtained with the ultrasonic sensor and with the wave probe for this condition was found to be within the 95 % confidence intervals (based on 29 independent averages), up to a frequency of 12 Hz. For this work, the calculation of the angular spreading function in section 5.3 and the estimation of the mean surface velocity in section 6, were based on frequencies below 9 Hz.

3 Data analysis with the WDM

3.1 *The wavelet directional method*

The WDM is based on a wavelet transform of the surface elevation measured in time at a set of locations distributed spatially (Donelan et al., 1996). In principle, the technique can be applied with any type of wavelet but the Morlet wavelet (Grossmann & Morlet, 1984) was found to provide better localization properties by Donelan et al. (1996). For this wavelet, there is a direct relation between the wavelet scale and the Fourier angular frequency ω (Meyers, Kelly, & O'Brien, 1993), which allows a direct comparison between the Morlet wavelet transform and the free surface spectrum (Massel, 2001). The Morlet wavelet transform at the scale that corresponds to the radian frequency ω, calculated at the location $\boldsymbol{r} = (x, y)$ and at discrete time t, where t varies between 0 and T with increments of $1/f_s$, f_s is the sampling frequency, and T is the measurement duration, is defined in Fourier space as (e.g., Torrence & Compo, 1998)

$$W(\omega, \boldsymbol{r}, t) = \frac{\pi^{1/4}}{(m\omega)^{1/2}} \sum_{\nu} \exp\left[-\frac{1}{2}\left(\Lambda - \frac{2\pi\omega_\nu}{m\omega}\right)^2 + \mathrm{i}\omega_\nu t\right] \tilde{\zeta}(\boldsymbol{r}, \omega_\nu), \tag{1}$$

where $\omega_\nu = \nu 2\pi/T$, $\nu = 0, \ldots, f_s T/2$ is an integer index, and $\tilde{\zeta}(\boldsymbol{r}, \omega_\nu)$ is the discrete Fourier transform in time of the elevation $\zeta(\boldsymbol{r}, t)$ measured at the location $\boldsymbol{r}$ and evaluated at the frequency ω_ν. Λ is a parameter that controls the width of the wavelet, which was equal to 6 for this study, and $m = 2\pi[(2+\Lambda^2)^{1/2} - \Lambda]$ is a frequency correction factor (Meyers et al., 1993). The width $\Lambda = 6$ was chosen in accordance with Torrence and Compo (1998), to allow an easier calculation of the confidence intervals. The wavelet transform is often measured at a set of logarithmically spaced frequencies. For this work, the set $\omega = \pi 2^{-2+l/4}$, where $l = 0, \ldots, 27$ is an integer index, was used. This resulted in four so-called voices (intermediate frequencies per octave) used for the analysis. The Morlet wavelet transform is a complex quantity, with phase defined as

$$\Phi(\omega, \boldsymbol{r}, t) = \tan^{-1}\left[\frac{\Im(W(\omega, \boldsymbol{r}, t))}{\Re(W(\omega, \boldsymbol{r}, t))}\right], \tag{2}$$

where $\Re$ and $\Im$ are the real and imaginary part of the transform, respectively.

The surface elevation ζ is represented as a quasi-stationary random process, so that its statistics are approximately stationary within the spatial separations L_x and L_y. The instantaneous streamwise and lateral components of the wavenumber, $k_x(\omega, t)$ and $k_y(\omega, t)$, respectively, of the waves with frequency ω, can be found as (Donelan et al., 1996)

$$k_x(\omega, t) = [\Phi(\omega, \boldsymbol{r}_B, t) - \Phi(\omega, \boldsymbol{r}_A, t)]/L_x, \tag{3a}$$

$$k_y(\omega, t) = [\Phi(\omega, \boldsymbol{r}_C, t) - \Phi(\omega, \boldsymbol{r}_A, t)]/L_y, \tag{3b}$$

respectively. The wavenumber modulus $k(\omega, t)$ and the direction of propagation with respect to the x-axis, $\theta(\omega, t)$, can be determined as

$$k(\omega, t) = [k_x^2(\omega, t) + k_y^2(\omega, t)]^{1/2}, \tag{4}$$

and

$$\theta(\omega, t) = \tan^{-1}\left[\frac{k_y(\omega, t)}{k_x(\omega, t)}\right], \tag{5}$$

respectively.

According to Donelan et al. (1996), an estimation of the directional frequency-wavenumber spectrum of the surface elevation can be obtained by conditionally averaging the scaled squared amplitudes of the wavelet transform computed at a given probe p, $|W(\omega, \boldsymbol{r}_p, t)|^2$, based on the value of the corresponding wavenumber $k(\omega, t)$ and angle $\theta(\omega, t)$. As a first step of the procedure, a finite set of values of the wavenumber, $k_i = (i + 0.5)\Delta k$, and of the angle of propagation, $\theta_j = (j + 0.5)\Delta\theta$, where i and j are integer indices, and Δk and $\Delta\theta$ are widths of intervals (bins), are defined. As a second step, each term of the wavelet transform at the frequency ω and at time t is analyzed. If the corresponding wavenumber, $k(\omega, t)$, and angle of propagation, $\theta(\omega, t)$, are within the intervals $|k(\omega, t) - k_i| \leq \Delta k/2$ and $|\theta(\omega, t) - \theta_j| < \Delta\theta/2$, then the squared transform $|W(\omega, \boldsymbol{r}_p, t)|^2$ is normalized and added to the spectrum $\chi(k_i, \theta_j, \omega)$. In mathematical terms, the spectrum is defined as

$$\chi(k_i, \theta_j, \omega) = \frac{1}{N\Delta k\Delta\theta} \sum_t |W(\omega, \boldsymbol{r}_p, t)|^2 \,;\ \text{if } |k(\omega, t) - k_i| \leq \frac{\Delta k}{2},\ |\theta(\omega, t) - \theta_j| \leq \frac{\Delta\theta}{2} \tag{6}$$

where $N = f_s T$ is the number of samples of the time-series of the surface elevation. According to a wave-packet representation of the free surface (Krogstad, 2005), the spectrum $\chi(k_i, \theta_j, \omega)$ can be seen as the probability of finding a wave packet with the wavenumber and angle of propagation included in the intervals represented by k_i and θ_j and with size Δk and $\Delta\theta$, respectively. The directional frequency spectrum is defined as

$$E(\omega, \theta_j) = \Delta k \sum_i \chi(k_i, \theta_j, \omega). \tag{7}$$

The frequency spectrum can be found as

$$S(\omega) = \Delta\theta \sum_j E(\omega, \theta_j). \tag{8}$$

The streamwise frequency-wavenumber spectrum $X(k_{x,i}, \omega)$ and the transverse frequency-wavenumber spectrum $Y(k_{y,i}, \omega)$ at the streamwise and transverse wavenumbers $k_{x,i}$ and $k_{y,i}$, respectively, can be calculated directly as

$$X(k_{x,i}, \omega) = \frac{1}{N\Delta k} \sum_t |W(\omega, \boldsymbol{r}_p, t)|^2 \,;\ \text{if } |k_x(\omega, t) - k_{x,i}| \leq \frac{\Delta k}{2}, \tag{9a}$$

$$Y(k_{y,i}, \omega) = \frac{1}{N\Delta k} \sum_t |W(\omega, \boldsymbol{r}_p, t)|^2 \,;\ \text{if } |k_y(\omega, t) - k_{y,i}| \leq \frac{\Delta k}{2}, \tag{9b}$$

respectively. With the normalization of the wavelet transform indicated in Eq. (1), χ, E, S, X, and Y are approximations of the corresponding Fourier power density spectra (e.g., Massel, 2001). Notice that, due to the configuration of the probes during the experiments, the calculation of the streamwise spectrum of Eq. (9a) only requires the measurements of the surface elevation at the two locations A and B, while the calculation of the transverse spectrum of Eq. (9b) only requires the measurements of the surface elevation at the locations A and C. In the rest of the paper, the subscripts i and j are omitted for simplicity.

One additional type of spectrum will be used for the analysis in the following sections. This spectrum, defined as $\chi_0(\theta)$, corresponds to the spectrum $\chi(k, \theta, \omega)$ evaluated at a certain wavenumber

k_0, i.e.,

$$\chi_0(\theta) = \int\int \chi(k,\theta,\omega)\delta(k-k_0)\delta[\omega-\Omega(k_0,\theta)]\mathrm{d}k\mathrm{d}\omega, \tag{10}$$

where δ is a Dirac delta function, and $\Omega(k_0,\theta)$ is the frequency of the surface waves with wavenumber k_0 and angle θ prescribed by a dispersion relation which will be introduced in section 4. $\chi_0(\theta)$ has a similar meaning as the so-called angular spreading function, or angular distribution function (Krogstad, 2005, p. 35). In section 5, $\chi_0(\theta)$ will be compared with the so-called Von Mises distribution (e.g., Mardia & Jupp, 2000, p. 36), which is defined as

$$\exp\{b[\cos(\theta-\pi)-1]\}, \tag{11}$$

where b is a constant that determines the width of the spreading. The definition of Eq. (11) has been adapted with respect to the standard one (Mardia & Jupp, 2000) to reflect the assumption that the maximum amplitude of the waves with wavenumber k_0 occurs at $\theta = \pi$. This assumption will be justified empirically in section 4. The function has also been normalized, so that its maximum is one.

3.2 *Uncertainties*

Based on a Taylor expansion of Eqs (3), (4), and (5), the relative uncertainty of the wavenumber k and the absolute uncertainty of the angle θ measured with the WDM are both proportional to the relative uncertainties of the probes distances, i.e., they both increase with L_x^{-1} and L_y^{-1}. The maximum absolute wavenumbers which can be calculated based on Eq. (3) without aliasing are $k_x^{\max} = \pi/L_x$ and $k_y^{\max} = \pi/L_y$, respectively. With the setup used for this study, the maximum wavenumbers were $k_x^{\max} = 121$ rad m^{-1} and $k_y^{\max} = 90$ rad m^{-1}. The uncertainty of the measurements of L_x and L_y was estimated to be approximately 1 mm, i.e., 3.9 % of L_x and 2.9 % of L_y. As a result, k could be measured with a maximum relative uncertainty of 3.9 %, while the uncertainty of θ was approximately 0.04 rad. These uncertainties are representative for a single monochromatic wave.

The WDM can be inaccurate when multiple waves coexist simultaneously with the same frequency but different wavenumbers or directions of propagation (Donelan et al., 1996). The uncertainty in this case can be estimated by substituting into Eq. (1) the spectrum of two monochromatic waves, $\tilde{\zeta}(\boldsymbol{r},\omega_\nu) = \tilde{\zeta}_0(\boldsymbol{r},\omega_\nu) + \tilde{\zeta}_1(\boldsymbol{r},\omega_\nu)$, where $\tilde{\zeta}_0(\boldsymbol{r},\omega_\nu) = a_0\exp(\mathrm{i}\boldsymbol{k}_0\cdot\boldsymbol{r})$ and $\tilde{\zeta}_1(\boldsymbol{r},\omega_\nu) = a_1\exp(\mathrm{i}\boldsymbol{k}_1\cdot\boldsymbol{r}+\mathrm{i}\phi)$, where a_0 and a_1 are the amplitudes of the two waves with wavenumbers $\boldsymbol{k}_0$ and $\boldsymbol{k}_1$, respectively, and ϕ is the difference between their initial phases. If the two waves have similar amplitudes, i.e., $|a_1/a_0| \sim 1$, then the phase of the wavelet transform has little physical meaning, and the WDM is of no use. If one of the two waves has a larger amplitude, i.e., $|a_1/a_0| \ll 1$, then the phase Φ calculated with Eq. (2) tends asymptotically to the phase of the dominant wave, and so do the wavenumber and the angle as calculated with Eqs (3)–(5). Expanding Eq. (2) in a Taylor series with respect to $|a_1/a_0| \ll 1$, one finds that the relative uncertainty of the phase difference is $|a_1/a_0|[\sin((\boldsymbol{k}_2-\boldsymbol{k}_1)\cdot\boldsymbol{r}-\phi)-\sin(\phi)] \leq |a_1/a_0|$. The relative uncertainty of k and the absolute uncertainty of θ can both be estimated as $|a_1/a_0|/(k_0L)$, where L is a characteristic distance between the probes, and k_0 is the wavenumber of the dominant wave. For the range of conditions investigated here, k_0L varied between 0.8 and 2.6. Assuming for example $|a_1/a_0| \sim 0.1$, the uncertainty of the wavenumber k_0 of the dominant wave was between 4 % and 13 %, while the uncertainty of the angle θ was between 0.04 rad and 0.13 rad.

The statistics of the frequency spectrum $S(\omega)$ calculated with Eq. (8) based on a Morlet wavelet transform with $\Lambda = 6$ have been analyzed by Torrence and Compo (1998). $S(\omega)$ is chi-squared distributed with a frequency-dependent number of degrees of freedom, which can be calculated as

(Torrence & Compo, 1998)

$$N_F = 2\left[1 + \left(\frac{m\omega N}{4.64\pi f_s}\right)^2\right]^{1/2}. \tag{12}$$

The uncertainty of the spectrum is smaller at high frequencies ω, where more samples are independent. The statistics of the spectra $\chi(k,\theta,\omega)$, $X(k_x,\omega)$, and $Y(k_y,\omega)$ have been discussed by Krogstad (2005, chapter 2.4). According to Eqs (6) and (9), these spectra are effectively averaged over the number of occurrences of the measured wavenumber, k_i, and angle, θ_j, within each corresponding interval. Krogstad (2005) did not provide a formula to calculate the confidence intervals. For this work, it was assumed that each spectrum calculated with the WDM is chi-squared distributed, similarly to the spectrum $S(\omega)$. The number of degrees of freedom was then calculated independently for each wavenumber and angle based on Eq. (12), but replacing N with the number of occurrences observed for each interval. Since this number is always smaller than N, wider confidence intervals are found for the spectra $\chi(k,\theta,\omega)$, $X(k_x,\omega)$, and $Y(k_y,\omega)$ compared to those for the frequency spectrum $S(\omega)$. In all cases, the confidence intervals are wider at low frequencies and become narrower if Δk and $\Delta\theta$ are increased. For the measurements reported here, where the total number of samples was $N = 29500$, the values $\Delta k = 2\pi$ rad m^{-1} and $\Delta\theta = \pi/10$ rad were chosen for the analysis. Examples of the resulting confidence intervals for the frequency spectrum $S(\omega)$ and for the spectrum $\chi_0(\theta)$ are shown in Fig. 2 and Fig. 6, respectively.

4 Free surface patterns of turbulent shallow flows

For a similar range of flow conditions as the one investigated in this study, Dolcetti et al. (2016, section V B) demonstrated that the dispersion relation of the free surface patterns can be approximated by the dispersion relation of gravity-capillary waves propagating in a flow where the time-averaged streamwise flow velocity varies like a power function of the depth, according to

$$U(z) = U_0\left(\frac{z}{d}\right)^n, \tag{13}$$

where z is the vertical co-ordinate normal to the flume bed. A value of $n = 1/3$ for the exponent was found to yield accurate results for the conditions investigated by Dolcetti et al. (2016, FIG. 1). Gravity-capillary waves are identified by a wavenumber $k = 2\pi/\lambda$, where λ is a wavelength, by the angle between their direction of propagation and the direction of the flow, θ, and by a phase velocity $c(k,\theta)$ relative to a static observer. Then, their angular frequency Ω can be calculated through the dispersion relation $\Omega(k,\theta) = kc(k,\theta)$. For an irrotational flow with constant velocity U_0, the phase velocity of gravity-capillary waves can be decomposed into the sum of the advection velocity, $U_0\cos(\theta)$, and the phase speed of gravity-capillary waves in still water,

$$c_0(k) = \left[\left(g + \frac{\gamma}{\rho}k^2\right)\frac{\tanh(kd)}{k}\right]^{1/2}, \tag{14}$$

where γ is the surface tension coefficient, ρ is the density of water, and g is the gravity constant. If the flow is sheared, this decomposition is not straightforward, since the dependence of c on the velocity gradient is nonlinear (e.g., Shrira, 1993). For a flow with a power-function velocity profile, the phase velocity of gravity waves was calculated numerically by means of the procedure described by Fenton (1973). Surface tension effects, neglected by Fenton (1973), were included for this study according to Eq. (7) of Dolcetti et al. (2016), although the shortest waves that could be measured

with the experimental setup described in section 2 had the wavenumber $k_y^{\max} = 90$ rad m^{-1}, therefore they were mainly affected by gravity. If the flow is only slightly sheared, i.e., the ratio $\Gamma/(kc_0)$ is small, where Γ is a representative value of shear, then the dependence of the dispersion relation on the shear is approximately linear. Then, the flow mainly induces a Doppler shift of the phase velocity with respect to an intrinsic phase speed, which at first order of $\Gamma/(kc_0)$ is not affected by the shear and coincides with the phase speed in still water, $c_0(k)$ (see Shrira, 1993, Eq. (4.2b)). As a result, the dispersion relation can be approximated as

$$\Omega(k,\theta) \approx k[G(k,d)U_0\cos(\theta) + c_0(k)], \tag{15}$$

where the influence of shear is expressed by the factor $G(k,d)$. $G = 1$ yields the expression valid for an irrotational flow.

If the effective Doppler shift velocity GU_0 is larger than the minimum of c_0, which is approximately 0.23 m s^{-1} for water, stationary waves with frequency $\Omega(k,\theta) = 0$ can form. These waves propagate upstream with a velocity that balances the advection by the flow, so that they appear static to an external observer. They are identified by the wavenumber k_0, which is in general a function of the angle θ. Stationary waves originate due to the presence of a fixed disturbance, such as an obstacle on the bed. An isolated disturbance produces stationary waves at different angles, which can form distinctive three-dimensional wake patterns away from the disturbance (e.g., Harband, 1976; Lacaze et al., 2013; Teixeira, Paci, & Belleudy, 2017). When the bed is homogeneously rough, these patterns may not form. One can see from Eqs (14) and (15) that stationary waves with an angle $\theta \neq \pi$ are generally shorter than the stationary waves with $\theta = \pi$, so that their interaction with the rough bed is weaker. Dolcetti et al. (2016) measured the dispersion relation of gravity-capillary waves over the same homogeneously rough bed used for the present study. In the flow conditions for which U_0 was larger than the minimum of Eq. (14), only stationary waves with the wavefront perpendicular to the flow direction (i.e., with $\theta = \pi$) were clearly observed, while waves with different orientations were found to be not stationary. These observations are confirmed in section 5 of this work. To simplify the notation, in this work k_0 indicates only the wavenumber of the stationary waves oriented directly against the current, with $\theta = \pi$. Then, for the velocity profile of Eq. (13), k_0 can be found as the numerical solution of (Burns, 1953)

$$k_0 \frac{\mathrm{I}_{-1/2-n}(k_0 d)}{\mathrm{I}_{1/2-n}(k_0 d)} = \frac{g + \frac{\gamma}{\rho}k_0^2}{U_0^2}, \tag{16}$$

where I_n is the modified Bessel function of order n. It should be noted that Eq. (16) is valid for generic values of shear, as opposed to Eq. (15). For a more general case where stationary waves with angles different from θ need to be taken into account, the quantity U_0 should be replaced by $U_0\cos(\pi - \theta)$ in Eq. (16) to yield the θ-dependent value of k_0.

The waves with wavenumber modulus $k = k_0$ calculated by Eq. (16), cannot be stationary if they are inclined at an angle $\theta \neq \pi$ with respect to the streamwise direction. Their frequency, $\Omega(k_0,\theta) = k_0 c(k_0,\theta) > 0$, can be calculated numerically with the procedure described by Fenton (1973). These waves (including the stationary wave with $\theta = \pi$ and $\Omega = 0$) were found to represent the strongest contribution to the wave field at low frequencies in the measurements reported by Dolcetti et al. (2016). In order to discuss the importance and possible origin of this pattern, an approximation of $\Omega(k_0,\theta)$ in analytical form is useful. While the approximate Eq. (15) applies to any wave, its solution depends on the factor $G(k,d)$, which is unknown in general. Hedges and Lee (1992) proposed to calculate an equivalent uniform current, represented here by $G(k,d)U_0$, by integrating the velocity profile over a distance $\tanh(kd)/k$ from the surface. An alternative estimation of $G(k,d)$ which is valid only for the waves with wavenumber $k = k_0$ is suggested here. $G(k = k_0, d)$ is indicated as G_0 for the rest of this paper. Based on the decomposition

of the dispersion relation following Eq. (15), G_0 is independent of the direction of propagation. Substituting k_0 in place of k in Eq. (15), using Eq. (16), and considering stationary waves with $\theta = \pi$ so that $\Omega(k_0, \pi) = 0$, G_0 can be calculated as

$$G_0 = \frac{c_0(k_0)}{U_0} = \left[\frac{\mathrm{I}_{-1/2-n}(k_0 d)}{\mathrm{I}_{1/2-n}(k_0 d)} \tanh(k_0 d)\right]^{1/2}. \tag{17}$$

As a result,

$$\Omega(k_0, \theta) = k_0 \left[U_0 G_0 \cos(\theta) + c_0(k_0)\right] \tag{18}$$

is the approximate dispersion relation of all waves with wavenumber modulus k_0, including non-stationary waves that propagate at the angle θ. Equation (18) coincides with the numerical solution obtained according to Fenton (1973) when $\theta = \pi$ and $\theta = \pm\pi/2$, in which case $\Omega(k_0, \pi) = 0$ and $\Omega(k_0, \pm\pi/2) = k_0 c_0(k_0)$, respectively. At different θ, the accuracy of Eq. (18) depends on the validity of Eq. (15), i.e., on the value of the parameter $\Gamma/(k_0 c_0(k_0))$. Using the velocity gradient at the surface as an estimate of the characteristic shear, $\Gamma = nU_0/d$, then the error of Eq. (18) should depend on $n/(G_0 k_0 d)$. Across the range of flow conditions used for this study (see Table 1), where $n = 1/3$, G_0 was found to vary between 0.97 in condition 2 to 0.91 in condition 13, while $k_0 d$ varied between 2.5 in condition 13 and 6.5 in condition 2. As a result $n/(G_0 k_0 d)$ was found to be between 0.05 and 0.14, with the larger value obtained at condition 13. The maximum difference between Eq. (18) and the numerical solution obtained according to Fenton (1973) was observed at $\theta = 0$, and varied between 0.09 % and 1.5 % of $k_0 c_0(k_0)$ across all flow conditions, with the larger value obtained at condition 13.

The waves with wavenumber k_0 were the longest waves observed in each condition by Dolcetti et al. (2016), and the only ones which were found to propagate at angles θ which differed from either $\theta = 0$ or $\theta = \pi$. Other waves observed by Dolcetti et al. (2016) were: (i) gravity-capillary waves that propagated downstream with the wavenumber $k > k_0$ and the angle $\theta = 0$, (ii) gravity-capillary waves with the wavenumber $k > k_0$ and with the angle $\theta = \pi$ which propagated upstream, and (iii) non-dispersive patterns moving at a constant velocity close to the mean surface velocity. The dispersion relation of the first type of waves could be calculated numerically with the procedure of Fenton (1973) while for the second type of waves that propagate upstream, this procedure can be unstable due to a singularity of the integrand function. Such a singularity occurs at the critical-layer depth, z_c, where $c(k, \theta) = U(z_c)\cos(\theta)$. For both types of waves propagating parallel to the x-direction, an approximation of the dispersion relation calculated for an irrotational flow is

$$\Omega(k, \theta) \approx k_x U_0 + k c_0(k), \tag{19}$$

where $k_x = k\cos(\theta)$. The frequency of the non-dispersive waves is

$$\Omega_0(k, 0) = k_x U_0. \tag{20}$$

Dolcetti et al. (2016, section IV) suggested that the non-dispersive waves may have been excited non-resonantly by turbulence according to the mechanism described by Teixeira and Belcher (2006) and in analogy with the experiments of Savelsberg and Van De Water (2009) and Longo (2010, 2011) on turbulence behind a grid or a Crump weir.

5 Experimental results

5.1 *Streamwise and transverse frequency-wavenumber spectra*

As a first step of the analysis, the ability of the WDM to estimate the spectra of the surface elevation was tested. Figure 2 shows the standard Fourier frequency spectrum of the elevation measured for flow condition 7 with wave probe A, and the estimation of the same spectrum obtained by Eq. (8) based on the WDM. Condition 7 had an intermediate Froude number, and it is believed to be representative of the average behavior of the water surface across the tested range of flow conditions. The spectrum obtained with the WDM is a smoother version of the Fourier spectrum, due to the convolution with the spectrum of the wavelets (Krogstad, 2005, p. 72). The Fourier spectrum was the average of 59 independent measurements, each obtained using a Hanning window with the length of 10 s, or 500 samples. The 95 % confidence intervals of the WDM surface spectrum were calculated based on Eq. (12). The uncertainty of the WDM spectrum is smaller than the uncertainty of the Fourier spectrum at frequencies larger than 1.4 rad s^{-1}. The two spectra are very similar over the whole range of frequencies, and their difference is comparable to the measurement uncertainty at each frequency.

The frequency-wavenumber spectra of the surface elevation obtained with the WDM for flow conditions 1 and 7 are shown in Figs 3a and 3b, and Figs 3c and 3d, respectively. These spectra can be compared visually with the results reported by Dolcetti et al. (2016) (their Figs. 11 and 9), which had been obtained for the same flow conditions using two arrays of 8 conductance wave probes, by means of a Fourier analysis. Figures 3a and 3c show the streamwise components of the frequency-wavenumber spectra, $X(k_x, \omega)$, while Figs 3b and 3d show the transverse components of the same spectra, $Y(k_y, \omega)$.

The black lines in Fig. 3 indicate the dispersion relations of the different types of gravity-capillary waves that were introduced in section 4. These relations were calculated by means of the numerical procedure described by Fenton (1973), for a flow with the mean velocity profile approximated by Eq. (13). The magenta lines in the same figure represent the approximate relations of Eqs (18) and (19), and the frequency of the non-dispersive waves, Eq. (20). The frequency-wavenumber spectra computed for condition 1, shown in Figs 3a and 3b, do not show the dispersion relation of the waves with wavenumber k_0, approximated by Eq. (18), as the stationary waves could not form in this condition. Instead, the streamwise spectrum $S(k_x, \omega)$ in Fig. 3a is dominated by the presence of non-dispersive patterns which follow Eq. (20). Dolcetti et al. (2016) and Savelsberg and Van De Water (2009) suggested that these patterns are caused by the interaction between turbulence and the free surface. At frequencies higher than approximately 20 rad s^{-1}, downstream-propagating gravity-capillary waves that follow the dispersion relation approximated by Eq. (19) with $k_x > 0$ are also visible in Fig. 3a. Upstream-propagating gravity-capillary waves with the similar dispersion relation but with $k_x < 0$ can be found at the frequencies between 10 rad s^{-1} and 20 rad s^{-1}, in the same figure. The transverse frequency-wavenumber spectrum shown in Fig. 3b for condition 1 shows a maximum at a transverse wavenumber of approximately zero at all frequencies, which suggests that the patterns on the free surface were mainly two-dimensional.

The dispersion relation of the three-dimensional distribution of waves with wavenumber modulus equal to k_0, Eq. (18), is represented by the dashed-dotted lines in Figs 3c and 3d. These waves dominate both the streamwise and the transverse spectra, in agreement with the observations by Dolcetti et al. (2016). The difference between the frequency of these waves obtained by means of the procedure described by Fenton (1973) and its approximation represented by Eq. (18) was smaller than 0.1 rad s^{-1} for the flow condition represented in Figs 3c and 3d, therefore it is difficult to distinguish the two corresponding lines in these figures. The downstream-propagating gravity-capillary waves with $k_x > k_0 = 52.4$ rad m^{-1} are also visible in Fig. 3c, where they are represented by the solid lines at the frequencies higher than approximately 50 rad s^{-1}. The upstream-propagating waves with $k_x > k_0$ are represented by the dotted line in Fig. 3c, in the range

of wavenumbers higher than approximately 50 rad m^{-1} and at the frequencies below approximately 20 rad s^{-1}. These waves are expected to appear at positive wavenumbers in spite of their angle of propagation $\theta \approx \pi$ because of the advection by the flow and of the symmetry of the frequency-wavenumber spectrum. In contrast with the results reported by Dolcetti et al. (2016) (see their Fig. 9), these waves cannot be observed in Fig. 3c. This fact can be explained based on the discussion in section 3.2, where it was shown that if two waves with similar frequency and different wavenumber coexist simultaneously, the WDM is able to identify only the wavenumber of the wave with the larger amplitude, with an accuracy which was estimated to be between 4 % and 13 % of k if the ratio between the two amplitudes is of the order $\mathcal{O}(0.1)$. This value is representative of the ratio between the spectrum of the upstream-propagating waves and that of the waves with wavenumber modulus k_0 at each frequency, according to the measurements of Dolcetti et al. (2016) (see their Fig. 9).

5.2 *Directional spectra*

In contrast with the analysis procedure implemented by Dolcetti et al. (2016), the WDM allows the calculation of the full three-dimensional spectrum of the surface elevation, $\chi(k, \theta, \omega)$. This spectrum characterizes completely the spatial and temporal behavior of the free surface, but is difficult to represent in two dimensions.

The directional frequency spectrum of the elevation calculated with Eq. (7) for flow condition 1 is shown in Fig. 4. This spectrum has a larger amplitude at the frequencies below 20 rad s^{-1}, and at the angle $|\theta| < \pi/2$. This range of frequencies and angles corresponds to the waves that propagate at a velocity near the mean surface velocity, which may have been generated by the interaction with turbulence. Two peaks at the frequency of approximately 20 rad s^{-1} and with the angles of $\pm\pi$ indicate the waves that propagate against the flow, which are responsible for the quasi-horizontal ridge of the streamwise frequency-wavenumber spectrum of Fig. 3a. Waves at higher frequencies had θ of approximately zero, therefore they propagated mainly downstream.

The directional frequency spectrum calculated for flow condition 7 is shown in Fig. 5a. This spectrum is compared with the dispersion relation of the radial distribution of waves with the wavenumber k_0, Eq. (18), expressed as a function of the angle of propagation θ. The waves with zero frequency correspond to stationary waves, which propagate against the flow direction with $\theta = \pi$. The waves with the frequency equal to or larger than $k_0[G_0U_0 + c_0(k_0)] \approx 50$ rad s^{-1} have θ which tends to zero, therefore they propagate mainly towards the positive streamwise direction. The spectrum at the intermediate frequencies follows closely the behavior represented by Eq. (18).

The spectrum of the waves with wavenumber k_0, $\chi_0(\theta)$, defined by Eq. (10), was investigated by interpolating the angular spectrum $\chi(k, \theta, \omega)$ on the plane $\omega = kG_0U_0\cos(\theta) + k_0c_0(k_0)$, which corresponds to the approximate dispersion relation of Eq. (18) for the waves with $k = k_0$. These waves are represented by the circle $k_x^2 + k_y^2 = k_0^2$ shown as a dashed line in Fig. 5b. The interpolated spectrum in Fig. 5b shows fair agreement with this circle, which suggests that the three-dimensional distribution of waves corresponds approximately to a circle with radius k_0 in wavenumber space. It should be noted that the spectral energy in Fig. 5b is not concentrated over this circle for all wavenumber angles, due to a strong predominance of the spectrum at the wavenumbers $k_x = -k_0$ and $k_y = 0$, which correspond to the angle $\theta = \pi$. Along the circle with radius k_0, the amplitude of the spectrum apparently decreases when $|\theta - \pi|$ increases.

5.3 *Directional spreading function*

For modeling purposes, it is useful to characterize the amplitude of the three-dimensional distribution of waves as a function of the angle of propagation, by means of the equivalent spreading function defined in section 3.1. The spectra $\chi_0(\theta)$ were estimated in terms of the values of the

interpolated frequency-wavenumber directional spectra (e.g., Fig. 5b), evaluated along the circle with $k_x^2 + k_y^2 = k_0^2$. The spectra were calculated only for flow conditions 3, 5, 7, 9, 10, 11, 12, and 13. In the remaining flow conditions, the measurement resolution was comparable to the wavelength $2\pi/k_0$, and the spectra were affected by aliasing. Examples of the spectra $\chi_0(\theta)$ obtained for conditions 7 and 11 are shown in Fig. 6, with the estimated 95 % confidence intervals obtained by means of the procedure outlined in section 3.2. The amplitude of the spectra has been scaled so to compare with the normalized spreading function of Eq. (11).

The logarithm of the spectrum $\chi_0(\theta)$ shown in Fig. 6 was found to increase almost linearly with the cosine of the angle $\theta - \pi$, in accordance with the behavior of the Von Mises spreading function of Eq. (11). In order to quantify the behavior of the measured spreading function, Eq. (11) was fitted to the measured $\chi_0(\theta)$ in semi-logarithmic co-ordinates using a weighted least-squares linear fitting. The weights corresponded to the equivalent number of degrees of freedom calculated based on Eq. (12), for each angle θ and frequency $\omega = \Omega(k_0, \theta)$. The number of samples N in Eq. (12) was replaced by the number of occurrences of the measured wavenumber within the interval of size Δk which contained the wavenumber k_0. This procedure was implemented in order to account for the larger uncertainty of the spectrum $\chi_0(\theta)$ at $\theta \approx \pi$, where $\Omega(k_0, \theta)$ is very small. For the flow conditions 3, 5, 7, 9, 10, 11, 12, and 13, the fitted value of b was found to be between 1.0 (for conditions 9, 12, and 13) and 1.9 (for conditions 7 and 10), with an average value of 1.4.

The values of b calculated for each of these flow conditions are reported in Table 1, along with the uncertainties of the least-squares fitting. These uncertainties were of the order of 20 % of b. Table 1 also reports the values of the characteristic wave steepness $k_0\sigma_\zeta$ for each condition. This parameter is often taken as a measure of the nonlinearities of the free surface (Phillips, 1960). Larger values of b (which indicate a narrower distribution) were observed in general for the conditions with a larger wave steepness. This result is discussed with more detail in section 7.

6 Estimation of the mean surface velocity

The measurements of the streamwise frequency-wavenumber spectra of the three-dimensional distribution of waves, obtained with the WDM based on a single pair of conductance wave probes, provide a procedure to estimate efficiently the mean surface velocity of the flow. The procedure is based on the approximate relation of Eq. (18), which indicates a linear dependence between the frequency $\Omega(k_0, \theta)$ and the streamwise component of the wavenumber $k\cos(\theta)$ for the waves with $k = k_0$. The factor of proportionality between these quantities, assuming $k_0 d \gg 1$ and therefore $G_0 \approx 1$, is approximately the mean surface velocity, U_0. For its validity, the estimation procedure requires that the mean surface velocity U_0 is larger than ≈ 0.23 m s^{-1}. At lower velocities, non-dispersive waves that move approximately at the mean surface velocity have been found to dominate the spectrum. U_0 could be estimated directly based on Eq. (20) in that case.

The procedure which allows to estimate U_0 based on a measurement of the WDM spectrum comprises of two steps. As a first step, the streamwise wavenumber k_x which corresponds to a maximum of the streamwise spectrum $X(k_x, \omega)$ at each frequency ω was identified using the Gaussian fitting procedure described by Herbert, Mordant, and Falcon (2010). According to this procedure, the measured streamwise spectrum $X(k_x, \omega)$ at each frequency ω was fitted with a Gaussian function of the streamwise wavenumber k_x, in order to identify the position of the maximum and the width of the Gaussian that provide the best fitting with the measurements. These two parameters identified the streamwise wavenumber of the spectral peak at each frequency, and a measure of the uncertainty of the fitting, respectively. As an example, the peaks of the spectrum identified in this way for flow condition 7 are shown in Fig. 7a with asterisks. Each peak relates a frequency ω with a specific streamwise wavenumber k_x. The peaks shown in Fig. 7a are approximately aligned along a straight line with slope $\approx U_0$, in agreement with Eq, (18). As a second step of the procedure, the mean surface velocity U_0 can then be estimated as the first-order coefficient of a linear fit through

the co-ordinates of the peaks.

The assumption $G_0 \approx 1$ is required by the proposed method, because G_0 is a function of U_0, which is unknown a priori. For improved accuracy, the Gaussian fitting should be performed in the range of wavenumbers between $-k_0$ and k_0, but these limits are also unknown. To provide a consistent approach through the different flow conditions investigated in this study, and also to take into account the larger uncertainty of the WDM at low frequencies, the linear fitting was limited in this study to the frequencies between 15 rad s^{-1} and 1.5 times the frequency of the first spectral peak with $k_x > 0$.

The results of the velocity estimation procedure applied to the experimental data are shown in Fig. 7b. In this figure, the estimated mean surface velocities are plotted against the measured values of U_0 for all flow conditions except condition 1. In this condition the proposed method did not apply, because U_0 was smaller than the minimum phase speed of gravity-capillary waves in still water. Excluding condition 13, where the uncertainty of the estimate was very large, the difference between the measured and estimated velocities was found to vary between 0.4 % in condition 3, to 13% in condition 4. The average relative error in the conditions from 2 to 12 was 8 %. The errorbars in Fig. 7b indicate the 95 % confidence intervals of the linear fitting of the spectral peaks, which depend mainly on the number of peaks which could be identified within the selected range of frequencies. The larger error in the conditions with larger mean surface velocity can be explained by the smaller characteristic frequencies of the surface waves for these conditions, which reduced the number of peaks that could be used for the linear fitting. Only three peaks were found for condition 13, which lead to the very large uncertainty of the estimate for this condition.

7 Discussion

The results obtained with the WDM presented in section 5 have confirmed and extended the results of a Fourier analysis applied by Dolcetti et al. (2016) in the same experimental conditions. Non-dispersive waves that are suggested to originate due to a non-resonant interaction with turbulence according to the theory of Teixeira and Belcher (2006) have been observed in the flow condition where the mean surface velocity was smaller than the minimum phase speed of gravity-capillary waves in still water. In the remaining flow conditions, radial distributions of stationary and non-stationary waves with the wavenumber k_0 of the stationary waves oriented against the current have been found to dominate the wave field. As a result, the wavelength $2\pi/k_0$ was found to represent the characteristic horizontal scale of the surface deformations for these conditions. Dolcetti et al. (2016) found that the spatial correlation function of the surface elevation had a fluctuation with the spatial period of approximately $2\pi/k_0$. Stationary waves can form also in a laminar flow, which suggests that the characteristic scales of the surface are not directly linked to turbulence. This observation differs from the results of Horoshenkov et al. (2013), who linked the period of the fluctuations of the correlation function with the characteristic size of turbulent eddies, in analogy with the results of Savelsberg and Van De Water (2009) and Longo (2011) obtained for strong turbulence behind a grid or a Crump weir. Nichols et al. (2016) proposed a theoretical model to explain the results of Horoshenkov et al. (2013). According to this model, localized deformations of the free surface are caused by the interaction with turbulent coherent structures, the spatial scale of the surface deformations is proportional to the scale of the turbulent structures, and the surface deformations fluctuate vertically in time, with a behavior similar to that proposed by Longo et al. (2013) for grid-stirred turbulence in still water. According to Nichols et al. (2016) the presence of a flow causes the advection of the surface oscillations at a velocity close to the mean surface velocity U_0. Oscillating patterns advected at the mean flow velocity were also observed by Fujita et al. (2011) and similarly linked to the effects of turbulence. In spite of their different interpretation, it is suggested that the patterns of waves observed in the present studies are similar to the ones observed by Horoshenkov et al. (2013), and that the results presented here may be relevant for a

wider range of flows, as discussed below.

In Fig. 8, the measured values of the characteristic surface scale reported by Horoshenkov et al. (2013) are compared with the theoretical values of the wavelength $2\pi/k_0$, calculated by means of Eq. (16) based on the mean surface velocity and mean flow depth reported by Nichols et al. (2016, Tab. 1), for the same experiments of Horoshenkov et al. (2013). The theoretical values of $2\pi/k_0$ calculated for the conditions investigated in the present work are also shown in Fig. 8, for reference. In this figure, the triangles and squares indicate the solution of Eq. (16) with $n = 1/3$, while the errorbars correspond to the solutions with $n = 1/2$ (shorter wavelength) and $n = 1/4$, respectively. The flow conditions investigated by Horoshenkov et al. (2013) had larger Froude numbers compared to the ones used for this work, therefore the values of $2\pi/k_0$ were more largely affected by the choice of the exponent of the velocity profile n. The dashed line indicates the wavelength of the stationary waves oriented against the flow calculated for an irrotational infinitely deep flow, $2\pi U_0^2/g$, and is also shown for reference. There is good agreement between the characteristic surface scale measured by Horoshenkov et al. (2013) and the wavelength $2\pi/k_0$. A larger error is found for the flow condition with a smaller characteristic wavelength of less than 0.1 m. This error may be explained by a smaller sensitivity of short waves to the presence of the rough bed, or by uncertainties in the calculation of the characteristic scale by Horoshenkov et al. (2013).

The relation between the characteristic surface scale obtained by Horoshenkov et al. (2013) based on the spatial period of the correlation function and the wavelength $2\pi/k_0$ can be understood by representing the free surface as a stationary linear random process defined by a complex Fourier angular amplitude spectrum $\hat{\zeta}(\theta)$. The dispersion relation of the three-dimensional distribution of waves with wavenumber k_0 can be approximated by Eq. (18). The surface elevation $\zeta(x, y, t)$ at the spatial co-ordinates x and y and at time t is then represented as

$$\zeta(x,y,t) = \frac{1}{2}\int_{-\pi}^{\pi} \hat{\zeta}(\theta) \mathrm{e}^{\mathrm{i}\{k_0[x\cos(\theta)+y\sin(\theta)]-\Omega(k_0,\theta)t\}} \mathrm{d}\theta + \text{c.c.}, \tag{21}$$

where c.c. indicates the complex conjugate of the first integral, which ensures that ζ is real-valued. $\hat{\zeta}(\theta)$ is a random function of the average spectrum $\chi_0(\theta)$ defined by Eq. (10),

$$\hat{\zeta}(\theta) = \xi(\theta)\left[\frac{2\chi_0(\theta)}{\Delta\theta}\right]^{1/2}, \tag{22}$$

where $\xi(\theta)$ is a normally distributed complex random variable. Savelsberg and Van De Water (2009) used an expression similar to Eq. (21) to describe gravity-capillary waves with a phase speed comparable to the speed of the flow, although in their case k_0 was representative of the dimension of columnar vortices from which the waves were assumed to originate. Substituting $\Omega(k_0, \theta)$ from Eq. (18) into Eq. (21), yields

$$\zeta(x,y,t) = \frac{\mathrm{e}^{-\mathrm{i}k_0c_0(k_0)t}}{2}\int_{-\pi}^{\pi} \hat{\zeta}(\theta) \mathrm{e}^{\mathrm{i}k_0[(x-G_0U_0t)\cos(\theta)+y\sin(\theta)]} \mathrm{d}\theta + \text{c.c.}, \tag{23}$$

which, if observed along the path $x = G_0U_0t \approx U_0t$, appears like a pattern that fluctuates vertically at the frequency of $k_0c_0(k_0) = k_0G_0U_0$. This behavior is in agreement with the model derived by Nichols et al. (2016). The correlation between two measurements of the surface elevation at the streamwise co-ordinates x and x' and at times t and $t' = t + (x' - x)/(G_0U_0)$ can be determined from Eq. (23) as

$$\left\langle \zeta^*(x,y,t)\zeta(x',y,t')\right\rangle = \left\langle \zeta^*(x,y,t)\zeta(x,y,t)\right\rangle \cos[k_0(x'-x)], \tag{24}$$

where the angular brackets represent ensemble averaging, and the asterisk the complex conjugate.

The correlation function described by Eq. (24) fluctuates along the line $t'-t = (x'-x)/(G_0U_0)$ with period $2\pi/k_0$. The behavior is in agreement with the observations by Horoshenkov et al. (2013). The additional decay of the correlation function observed by Horoshenkov et al. (2013) could be explained by the presence of non-dispersive waves and of the waves with $k > k_0$ that propagate parallel to the flow. These waves, also observed in section 5.1 and represented by Eqs (19) and (20), have not been considered in the simplified model expressed by Eq. (23). This model appears to justify the results of Horoshenkov et al. (2013) obtained over a different range of flow conditions and with a different rough bed than in this study. The wavelength of the stationary waves $2\pi/k_0$ was representative of the characteristic scale of the surface deformation measured by Horoshenkov et al. (2013), although Horoshenkov et al. (2013) had suggested a direct scaling with turbulence. Stationary waves can occur also without turbulence in a subcritical flow with a rough static bed, when the surface velocity is larger than the minimum of c_0. In these conditions, the fact that the characteristic surface scale could be estimated based on a purely laminar theory suggests that the interaction with the rough bed may be predominant over the direct effects of turbulence.

While the generation of stationary waves in a flow over a rough bed is well understood, the reason for the predominance of both stationary and non-stationary waves with wavenumber k_0 still needs to be clarified. A detailed theoretical explanation for these phenomena is beyond the scope of this work. An hypothesis can only be postulated based on a theory derived by Zakharov and Shrira (1990) under assumptions that are not rigorously satisfied in the case investigated here. It should be noted that the interaction with a rough bed can cause the emergence of both stationary and non-stationary waves, and the latter can have a wide range of wavenumber moduli and angles (Harband, 1976). Considering weak nonlinearity of the surface elevation, a triad of waves with wavenumber vectors $\boldsymbol{k}_0$, $\boldsymbol{k}_1$, and $\boldsymbol{k}_2$, and with frequencies Ω_0, Ω_1, and Ω_2, where $\boldsymbol{k} = k\cos(\theta)\boldsymbol{e}_x + k\sin(\theta)\boldsymbol{e}_y$ and $\boldsymbol{e}_x$, $\boldsymbol{e}_y$ are the unit vectors in the directions x and y, respectively, can exchange energy whenever $\boldsymbol{k}_0 = \pm\boldsymbol{k}_1 \pm \boldsymbol{k}_2$ and $\Omega_0 = \pm\Omega_1 \pm \Omega_2$ (Phillips, 1960). The first wave is chosen to be a stationary wave with $\boldsymbol{k}_0 = -k_0\boldsymbol{e}_x$ and $\Omega_0 = 0$, which originates due to the presence of the rough bed. The second wave is a non-stationary wave with wavenumber modulus k_0 that propagates at the angle θ so that $\boldsymbol{k}_1 = k_0\cos(\theta)\boldsymbol{e}_x + k_0\sin(\theta)\boldsymbol{e}_y$, and with the dispersion relation approximated as (Eq. (18)) $\Omega_1 = k_0G_0U_0\cos(\theta) + k_0c_0(k_0)$, where $G_0 = c_0(k_0)/U_0$. Then, a resonant interaction is possible with a third wave that has $\boldsymbol{k}_2 = \boldsymbol{k}_1 - \boldsymbol{k}_0$ and $\Omega_2 = \Omega_1 - \Omega_0$. The velocity of this wave along the x-direction is $\Omega_2/[k_0(1+\cos(\theta))] = G_0U_0$, therefore the wave cannot be a freely propagating gravity-capillary wave. Since $G_0U_0 < U_0$, it is possible in general to identify a critical depth z_c, for which $U(z_c) = G_0U_0$. Then, according to Zakharov and Shrira (1990), the third interacting wave can be replaced by a disturbance at the critical layer. The existence of a critical layer is also a requisite for the resonant interaction of the surface waves with turbulence, according to Teixeira and Belcher (2006). Therefore, it is suggested that a stationary wave can also mediate the transfer of energy between a non-stationary wave with wavenumber k_0 and angle θ, and a turbulent mode with wavenumber $|\boldsymbol{k}_1 - \boldsymbol{k}_0| = k_0[2+2\cos(\theta)]^{1/2}$. This mechanism could allow the selective growth of the waves with $k \approx k_0$ which can propagate at all angles.

A mechanism like the one described above has been found to allow the exchange of energy between two non-stationary surface waves and a vorticity wave (Drivas & Wunsch, 2016), or an internal wave (Thorpe, 1966). According to Zakharov and Shrira (1990) this mechanism can be responsible for the generation of the angular spectrum of wind waves in the ocean. This spectrum, initially narrow, can broaden due to the interaction with a critical layer if the primary wave propagates against the current, causing the formation of the angular spreading. In section 5.3, a larger characteristic wave steepness (which suggests stronger nonlinearity) was associated with a narrower spectrum. This result seems to disprove the validity of the mechanism described by Zakharov and Shrira (1990) for the conditions of the present study. The theory of Zakharov and Shrira (1990) was based on an expansion with respect to the parameter U_0/c_0 assumed small, whereas in the case investigated here $U_0/c_0 = G_0^{-1} \approx 1$. When $G_0 \approx 1$, the critical layer is in close proximity of the free surface, therefore the interactions can be potentially strong even for waves with small steepness. It is suggested that

additional parameters which could not be quantified for this study, such as the strength of turbulent pressure fluctuations, may affect the angular spreading. Further theoretical studies are needed in order to demonstrate the significance of these observations and to probe the hypothesis formulated in this section.

8 Conclusions

The experimental results in this paper have demonstrated the applicability of the wavelet directional method for the characterization of the free surface for a range of subcritical turbulent open-channel flows over a rough bed, in a laboratory flume. The method requires a small number of sensors capable of measuring the surface elevation across a small area, and applies to weakly non stationary processes, therefore it is particularly suited for non-contact monitoring of the flow conditions of rivers and open channel flows. The application of the WDM allowed the first known measurement of the three dimensional spectrum of the free surface of turbulent flows, shown in section 5.2. These measurements can improve the existing models of the surface shape and dynamics in rivers and open channels, and inform the development of accurate remote sensing techniques (e.g., Legleiter et al., 2017).

For the range of subcritical flow conditions investigated in this study, three types of waves have been found to dominate the surface spectra. At low flow velocities, the dominant waves were non-dispersive waves which are believed to originate from a non-resonant interaction with turbulence (Teixeira & Belcher, 2006). At higher velocities where stationary waves could form, radial distributions of stationary and non-stationary waves with the same wavelength dominated the spectra. The wavelength of the stationary waves aligned against the flow direction has been found to represent the characteristic scale of the surface, in apparent contrast with previous studies (Horoshenkov et al., 2013; Nichols et al., 2016) which had suggested a stronger link with turbulence at all flow conditions. A comparison with the data reported by Horoshenkov et al. (2013), discussed in section 7, has provided additional evidence in support of the results in the present work. A mechanism that could explain the occurrence of the complex patterns of waves observed in this study based on a theory developed by Zakharov and Shrira (1990) has been suggested. However, further theoretical studies are needed to investigate the significance of this mechanism.

A procedure that enables the estimation of the flow mean surface velocity based on a fitting of the streamwise frequency-wavenumber spectra has been proposed in section 6. The procedure is valid under the conditions that the three-dimensional patterns of waves are measurable, and follow the approximate dispersion relation introduced in Eq. (18). The technique accounts for the presence of gravity-capillary waves, but contrarily to Fourier-based methods it does not need large measurement areas. By allowing to take into account gradual variations of the bed elevation and flow velocity, the technique could have applications also beyond the homogeneous conditions considered in this work. The sensors only need to be able to measure the surface elevation at two separate locations, which can be obtained remotely. The method provided estimates of the velocity with an error of 8 % in average across the range of tested flow conditions.

Acknowledgements

The authors are grateful to Prof. Francisco J. Ocampo Torres for fostering the collaboration which resulted in this paper, and to Prof. Kirill V. Horoshenkov for his helpful comments on the first version of the manuscript. The authors are also grateful to three anonymous reviewers for their useful comments on the manuscript.

Notation

b = width parameter of the Von Mises distribution (–)
c = absolute phase velocity of waves (m s^{-1})
c_0 = phase speed in still water (m s^{-1})
d = mean depth (m)
E = directional frequency spectrum (m^2 s rad^{-2})
f_s = sampling frequency (s^{-1})
F = Froude number (–)
g = gravity acceleration (m s^{-2})
G = Doppler shear correction (–)
G_0 = Doppler shear correction for the waves with wavenumber k_0 (–)
k = wavenumber (rad m^{-1})
k_x = streamwise wavenumber (rad m^{-1})
k_y = transverse wavenumber (rad m^{-1})
k_0 = wavenumber of the stationary waves oriented against the flow (rad m^{-1})
L_x = streamwise distance between probes (m)
L_y = transverse distance between probes (m)
m = scale-frequency conversion factor (–)
n = exponent of the power-function velocity profile (–)
N = number of samples (–)
N_F = number of degrees of freedom (–)
$\boldsymbol{r}$ = co-ordinate vector (m)
R = Reynolds number (–)
S = frequency spectrum (m^2 s rad^{-1})
t = time (s)
T = measurement duration (s)
U_0 = mean surface velocity (m s^{-1})
W = Morlet wavelet transform (m $s^{1/2}$ $rad^{-1/2}$)
X = streamwise frequency-wavenumber spectrum (m^3 s rad^{-2})
Y = transverse frequency-wavenumber spectrum (m^3 s rad^{-2})
γ = surface tension coefficient (kg s^2)
Γ = characteristic flow shear (s^{-1})
ζ = surface elevation (m)
$\hat{\zeta}$ = angular amplitude spectrum of the surface (m rad^{-1})
$\tilde{\zeta}$ = Fourier transform in time of the elevation (m)
θ = angle of propagation (rad)
Λ = width of wavelet (–)
ρ = water density (kg m^{-3})
σ_ζ = standard deviation of the surface elevation (m)
Φ = phase of the Morlet wavelet transform (rad)
χ = three-dimensional frequency-wavenumber spectrum (m^3 s rad^{-3})
χ_0 = spectrum of the waves with wavenumber k_0 (m^2 rad^{-1})
ω = radian frequency (rad s^{-1})
Ω = dispersion relation (rad s^{-1})

References

Borue, V., Orszag, S. A., & Staroselsky, I. (1995). Interaction of surface waves with turbulence:

direct numerical simulations of turbulent open-channel flow. *Journal of Fluid Mechanics*, *286*, 1–23.

Brocchini, M., & Peregrine, D. H. (2001). The dynamics of strong turbulence at free surfaces. Part 1. Description. *Journal of Fluid Mechanics*, *449*, 225–254.

Burns, J. (1953). Long waves in running water. *Mathematical Proceedings of the Cambridge Philosophical Society*, *49*(04), 695–706.

Chiapponi, L., Longo, S., & Tonelli, M. (2012). Experimental study on oscillating grid turbulence and free surface fluctuation. *Experiments in Fluids*, *53*(5), 1515–1531.

Cobelli, P. J., Maurel, A., Pagneux, V., & Petitjeans, P. (2009). Global measurement of water waves by Fourier transform profilometry. *Experiments in Fluids*, *46*(6), 1037–1047.

Dolcetti, G., Horoshenkov, K. V., Krynkin, A., & Tait, S. J. (2016). Frequency-wavenumber spectrum of the free surface of shallow turbulent flows over a rough boundary. *Physics of Fluids*, *28*(10), 105105.

Dolcetti, G., & Krynkin, A. (2017). Doppler spectra of airborne ultrasound forward scattered by the rough surface of open channel turbulent water flows. *The Journal of the Acoustical Society of America*, *142*(5), 3122–3134.

Dolcetti, G., Krynkin, A., & Horoshenkov, K. V. (2017). Doppler spectra of airborne sound backscattered by the free surface of a shallow turbulent water flow. *The Journal of the Acoustical Society of America*, *142*(6), 3387–3401.

Donelan, M. A., Drennan, W. M., & Magnusson, A. K. (1996). Nonstationary analysis of the directional properties of propagating waves. *Journal of Physical Oceanography*, *26*(9), 1901–1914.

Drivas, T. D., & Wunsch, S. (2016). Triad resonance between gravity and vorticity waves in vertical shear. *Ocean Modelling*, *103*, 87–97.

Fenton, J. D. (1973). Some results for surface gravity waves on shear flows. *IMA Journal of Applied Mathematics*, *12*(1), 1–20.

Fujita, I., Furutani, Y., & Okanishi, T. (2011). Advection features of water surface profile in turbulent open-channel flow with hemisphere roughness elements. *Visualization of Mechanical Processes: An International Online Journal*, *1*(4).

Grossmann, A., & Morlet, J. (1984). Decomposition of Hardy functions into square integrable wavelets of constant shape. *SIAM Journal on Mathematical Analysis*, *15*(4), 723–736.

Guo, X., & Shen, L. (2010). Interaction of a deformable free surface with statistically steady homogeneous turbulence. *Journal of Fluid Mechanics*, *658*, 33–62.

Harband, J. (1976). Three dimensional flow over a submerged object. *Journal of Engineering Mathematics*, *10*(1), 1–21.

Hedges, T. S., & Lee, B. W. (1992). The equivalent uniform current in wave-current computations. *Coastal engineering*, *16*(3), 301–311.

Herbert, E., Mordant, N., & Falcon, E. (2010). Observation of the nonlinear dispersion relation and spatial statistics of wave turbulence on the surface of a fluid. *Physical Review Letters*, *105*(14), 144502.

Horoshenkov, K. V., Nichols, A., Tait, S. J., & Maximov, G. A. (2013). The pattern of surface waves in a shallow free surface flow. *Journal of Geophysical Research: Earth Surface*, *118*(3), 1864–1876.

Krogstad, H. E. (2005). The directional wave spectrum. In D. Hauser, K. K. Kahma, H. E. Krogstad, S. Lehner, J. Monbaliu, & L. R. Wyatt (Eds.), *COST Action 714, Measuring and Analysing the Directional Spectra of Ocean Waves.* Luxembourg: Office for Official Publications of the European Communities.

Krynkin, A., Horoshenkov, K. V., & Van Renterghem, T. (2016). An airborne acoustic method to reconstruct a dynamically rough flow surface. *The Journal of the Acoustical Society of America*, *140*(3), 2064–2073.

Lacaze, L., Paci, A., Cid, E., Cazin, S., Eiff, O., Esler, J. G., & Johnson, E. R. (2013). Wave

patterns generated by an axisymmetric obstacle in a two-layer flow. *Experiments in fluids*, *54*(12), 1618.

Legleiter, C. J., Mobley, C. D., & Overstreet, B. T. (2017). A framework for modeling connections between hydraulics, water surface roughness, and surface reflectance in open channel flows. *Journal of Geophysical Research: Earth Surface*, *122*(9), 1715–1741.

Longo, S. (2010). Experiments on turbulence beneath a free surface in a stationary field generated by a Crump weir: Free-surface characteristics and the relevant scales. *Experiments in Fluids*, *49*(6), 1325–1338.

Longo, S. (2011). Experiments on turbulence beneath a free surface in a stationary field generated by a Crump weir: Turbulence structure and correlation with the free surface. *Experiments in Fluids*, *50*(1), 201–215.

Longo, S. (2012). Wind-generated water waves in a wind tunnel: Free surface statistics, wind friction and mean air flow properties. *Coastal Engineering*, *61*, 27–41.

Longo, S., Chiapponi, L., & Liang, D. (2013). Analytical study of the water surface fluctuations induced by grid-stirred turbulence. *Applied Mathematical Modelling*, *37*(12), 7206–7222.

Mardia, K. V., & Jupp, P. E. (2000). *Directional Statistics*. New York, NY: Wiley.

Massel, S. R. (2001). Wavelet analysis for processing of ocean surface wave records. *Ocean Engineering*, *28*(8), 957–987.

Meyers, S. D., Kelly, B. G., & O'Brien, J. J. (1993). An introduction to wavelet analysis in oceanography and meteorology: With application to the dispersion of Yanai waves. *Monthly Weather Review*, *121*(10), 2858–2866.

Milan, D. J., Heritage, G. L., Large, A. R. G., & Entwistle, N. S. (2010). Mapping hydraulic biotopes using terrestrial laser scan data of water surface properties. *Earth Surface Processes and Landforms*, *35*(8), 918–931.

Nichols, A., Tait, S. J., Horoshenkov, K. V., & Shepherd, S. J. (2013). A non-invasive airborne wave monitor. *Flow Measurement and Instrumentation*, *34*, 118–126.

Nichols, A., Tait, S. J., Horoshenkov, K. V., & Shepherd, S. J. (2016). A model of the free surface dynamics of shallow turbulent flows. *Journal of Hydraulic Research*, *54*(5), 516–526.

Phillips, O. M. (1960). On the dynamics of unsteady gravity waves of finite amplitude Part 1. The elementary interactions. *Journal of Fluid Mechanics*, *9*(2), 193–217.

Savelsberg, R., & Van De Water, W. (2009). Experiments on free-surface turbulence. *Journal of Fluid Mechanics*, *619*, 95.

Shrira, V. I. (1993). Surface waves on shear currents: Solution of the boundary-value problem. *Journal of Fluid Mechanics*, *252*, 565–584.

Tamburrino, A., & Martínez, N. (2017). Wave and wind effects on the oxygen transfer across an air-water interface: An experimental study. *The Canadian Journal of Chemical Engineering*, *95*(8), 1594–1604.

Teixeira, M. A. C., & Belcher, S. E. (2006). On the initiation of surface waves by turbulent shear flow. *Dynamics of Atmospheres and Oceans*, *41*(1), 1–27.

Teixeira, M. A. C., Paci, A., & Belleudy, A. (2017). Drag produced by waves trapped at a density interface in non-hydrostatic flow over an axisymmetric hill. *Journal of the Atmospheric Sciences*, *74*, 1839–1857.

Thorpe, S. A. (1966). On wave interactions in a stratified fluid. *Journal of Fluid Mechanics*, *24*(4), 737–751.

Torrence, C., & Compo, G. P. (1998). A practical guide to wavelet analysis. *Bulletin of the American Meteorological society*, *79*(1), 61–78.

Turney, D. E., & Banerjee, S. (2013). Air–water gas transfer and near-surface motions. *Journal of Fluid Mechanics*, *733*, 588–624.

Wang, H., Felder, S., & Chanson, H. (2014). An experimental study of turbulent two-phase flow in hydraulic jumps and application of a triple decomposition technique. *Experiments in Fluids*, *55*(7), 1775.

Wang, H., Murzyn, F., & Chanson, H. (2015). Interaction between free-surface, two-phase flow and total pressure in hydraulic jump. *Experimental Thermal and Fluid Science*, *64*, 30–41.

Zakharov, V. E., & Shrira, V. I. (1990). Formation of the angular spectrum of wind waves. *Journal of Experimental and Theoretical Physics*, *71*, 1091–1100.

List of tables

List of figures

mean surface velocity, U_0. The solid line indicates exact estimation. The dashed lines indicate the estimated uncertainty of the surface velocity measurements, ± 3.5 %. The errorbars indicate the 95 % confidence intervals of the linear fitting through the spectral peaks, for each flow condition.

Figure 8 Comparison between (blue ellipses) the characteristic wavelength of the surface fluctuations estimated by Horoshenkov et al. (2013), and the wavelength $2\pi/k_0$ of the stationary waves oriented against the flow, determined theoretically with Eq. (16) for (black triangles) the conditions measured by Horoshenkov et al. (2013), and (red squares) for the conditions used for the present study, with the velocity profile exponent $n = 1/3$. The errorbars indicate the values obtained using $n = 1/2$ (lower values) and $n = 1/4$ (upper values). The dashed line indicates the wavelength of the stationary waves calculated for a deep, irrotational flow, $2\pi/k_0 = 2\pi U_0^2/g$. The semiaxes of the ellipses represent the uncertainty of the measurements reported by Horoshenkov et al. (2013).

Table 1 Tested flow conditions.

Flow condition	d (mm)	U_0 (m s^{-1})	F (–)	R (–)	σ_ζ (mm)	$2\pi/k_0$** (mm)	$k_0\sigma_\zeta$ (–)	b* (–)
1	42.2	0.19	0.30	8.0×10^3	0.05	-	-	-
2	72.9	0.35	0.41	2.5×10^4	0.40	70.0	3.6×10^{-2}	-
3	101.0	0.41	0.41	4.1×10^4	0.50	98.8	3.2×10^{-2}	1.4 ± 0.2
4	42.2	0.30	0.47	1.3×10^4	0.25	47.8	3.3×10^{-2}	-
5	101.3	0.49	0.49	4.9×10^4	1.79	139.3	8.1×10^{-2}	1.8 ± 0.4
6	43.0	0.34	0.52	1.5×10^4	0.49	63.0	4.9×10^{-2}	-
7	73.1	0.46	0.54	3.4×10^4	1.21	119.8	6.4×10^{-2}	1.9 ± 0.3
8	40.5	0.36	0.57	1.5×10^4	0.34	70.2	3.0×10^{-2}	-
9	43.4	0.40	0.61	1.7×10^4	0.46	86.5	3.3×10^{-2}	1.0 ± 0.3
10	99.0	0.60	0.61	5.9×10^4	2.03	200.4	6.4×10^{-2}	1.9 ± 0.4
11	72.4	0.54	0.64	3.9×10^4	1.17	159.3	4.6×10^{-2}	1.3 ± 0.2
12	43.1	0.43	0.66	1.8×10^4	0.57	98.5	3.6×10^{-2}	1.0 ± 0.2
13	73.2	0.58	0.68	4.2×10^4	1.10	180.4	3.8×10^{-2}	1.0 ± 0.4

*The uncertainties of b represent 95 % confidence intervals.

**$2\pi/k_0$ is the wavelength of the stationary waves aligned against the flow.

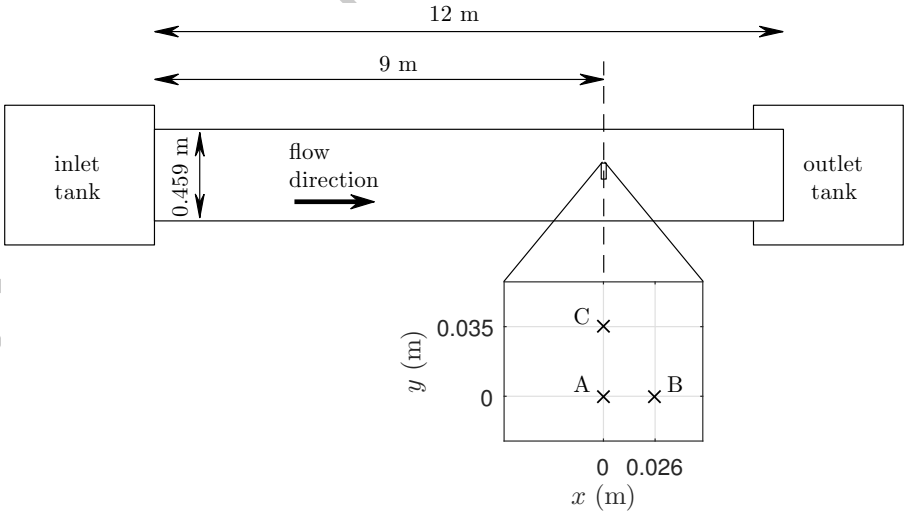

Figure 1 Schematic of the experimental flume. The inset shows the spatial arrangement of the three conductance wave probes.

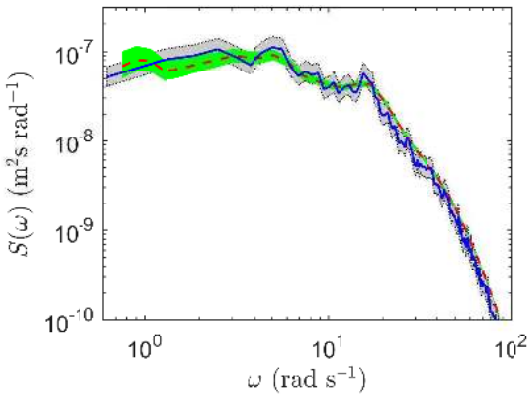

Figure 2 Comparison between (solid, blue) Fourier and (dashed, red) WDM frequency spectra of the surface elevation, Eq. (8), for flow condition 7. 95 % confidence intervals are indicated by the gray area for the Fourier spectrum (118 degrees of freedom) and by the green area for the WDM spectrum. The number of degrees of freedom for the WDM spectrum was calculated with Eq. (12), $N = 29500$ samples.

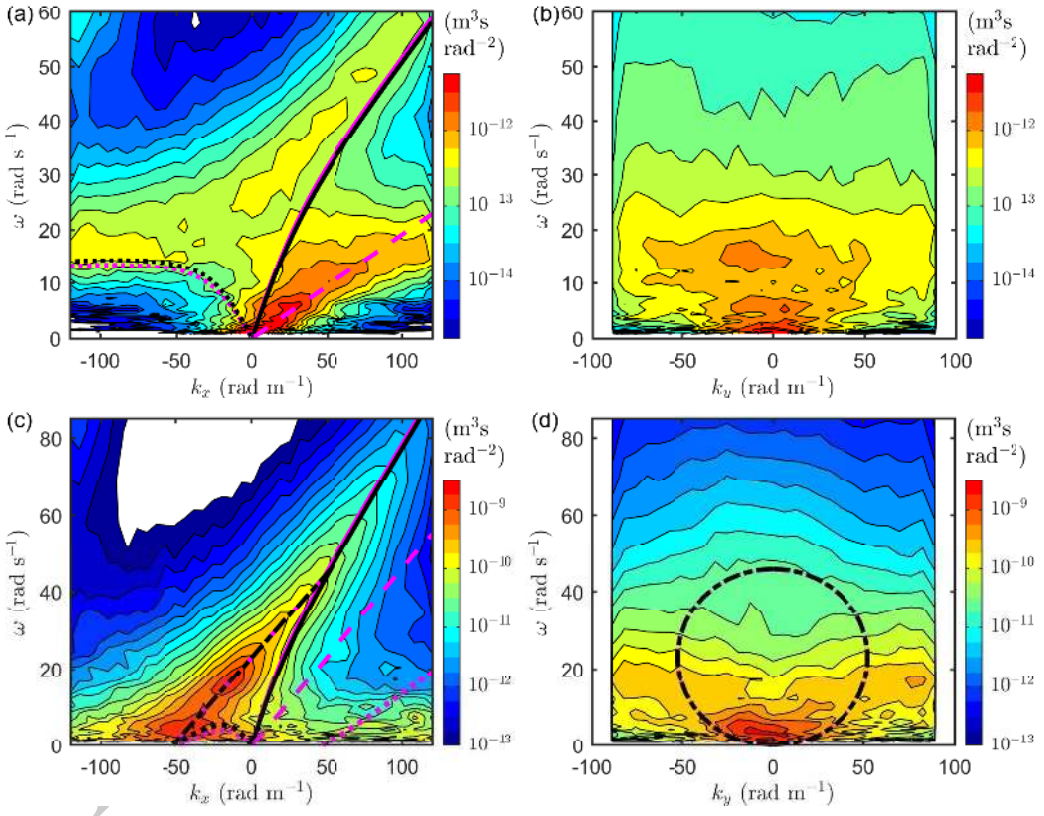

Figure 3 Example of the (a–c) streamwise and (b–d) transverse frequency-wavenumber spectra of the surface elevation, $X(k_x, \omega)$ and $Y(k_y, \omega)$, respectively, for flow conditions (a–b) 1, and (c–d) 7. Magenta lines represent the (dashed) frequency of non-dispersive patterns, Eq. (20); (solid) dispersion relation of downstream-propagating gravity-capillary waves for an irrotational flow, Eq. (19) with $k_x > 0$; (dotted) dispersion relation of upstream-propagating gravity-capillary waves for an irrotational flow, Eq. (19) with $k_x < 0$; (dashed-dotted) approximate dispersion relation of the radial distribution of waves with wavenumber modulus k_0, Eq. (18). Black lines are the corresponding dispersion relations obtained with the numerical procedure of Fenton (1973). The difference between the frequencies of the radial distribution of waves obtained according to Fenton (1973) (black, dashed-dotted) and approximated by Eq. (18) (magenta, dashed-dotted) was less than 0.1 rad s^{-1}, therefore these two lines in (c–d) are hard to distinguish from each other.

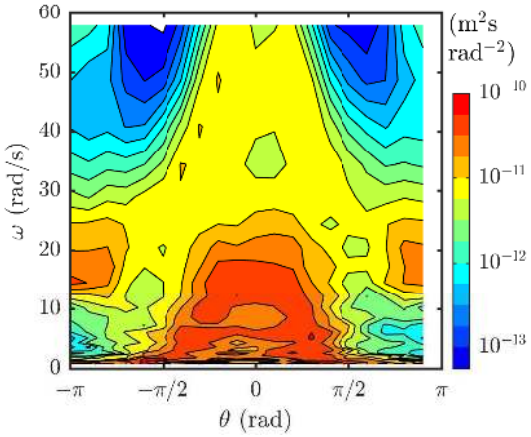

Figure 4 Directional frequency spectrum, $E(\omega, \theta)$, for condition 1.

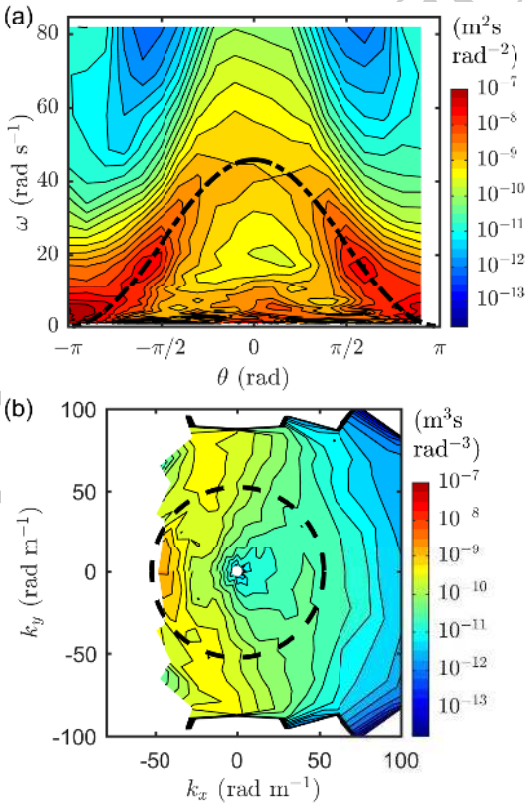

Figure 5 (a) Directional frequency spectrum, $E(\omega, \theta)$, and (b) projection of the three-dimensional spectrum $\chi(k, \theta, \omega)$ on the plane $\omega = kGU_0 \cos(\theta) + k_0 c_0(k_0)$, for condition 7. Lines represent (dashed-dotted) Eq. (18) and (dashed) $k_x^2 + k_y^2 = k_0^2$.

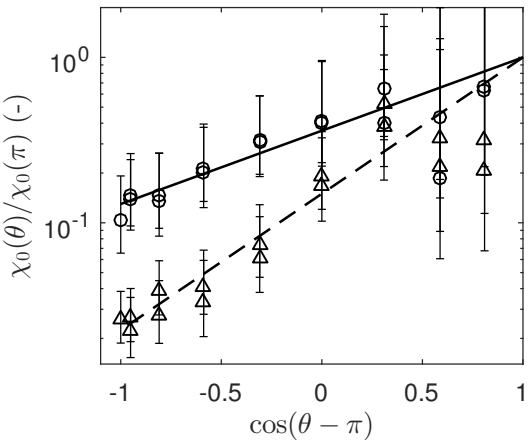

Figure 6 Examples of the scaled angular spreading function of the waves with wavenumber k_0, $\chi_0(\theta)/\chi_0(\pi)$, calculated for conditions (triangles) 7 and (circles) 12. The lines represent the Von Mises distribution (Eq. (11)) with (dashed) $b = 1.9$, and (solid) $b = 1.0$. The errorbars indicate the 95 % confidence intervals of the spectrum $\chi_0(\theta)$ calculated at each angle.

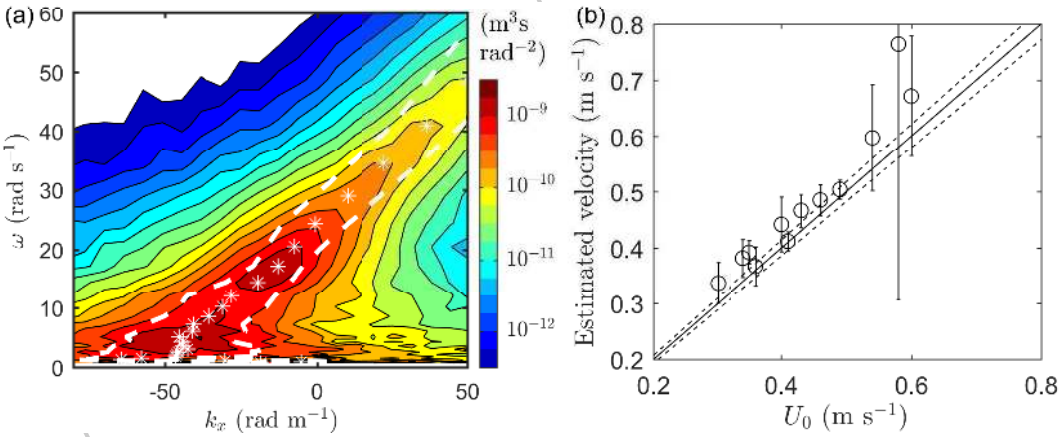

Figure 7 (a) Gaussian fitting of the measured streamwise frequency-wavenumber spectrum, for flow condition 7. The asterisks indicate the best-fit wavenumber k_x, at each frequency ω. The dashed lines are displaced horizontally by an amount equal to the width of the fitted Gaussian function. (b) Mean surface velocity estimated with the suggested procedure, plotted against the measured mean surface velocity, U_0. The solid line indicates exact estimation. The dashed lines indicate the estimated uncertainty of the surface velocity measurements, ±3.5 %. The errorbars indicate the 95 % confidence intervals of the linear fitting through the spectral peaks, for each flow condition.

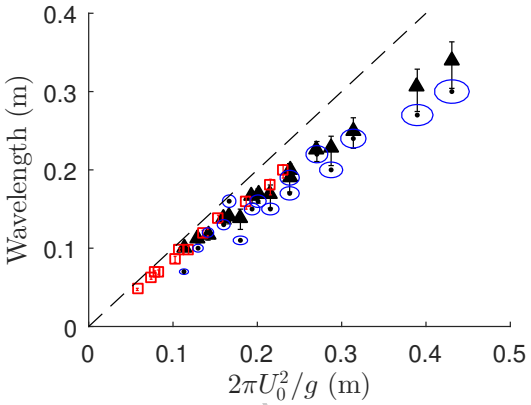

Figure 8 Comparison between (blue ellipses) the characteristic wavelength of the surface fluctuations estimated by Horoshenkov et al. (2013), and the wavelength $2\pi/k_0$ of the stationary waves oriented against the flow, determined theoretically with Eq. (16) for (black triangles) the conditions measured by Horoshenkov et al. (2013), and (red squares) for the conditions used for the present study, with the velocity profile exponent $n = 1/3$. The errorbars indicate the values obtained using $n = 1/2$ (lower values) and $n = 1/4$ (upper values). The dashed line indicates the wavelength of the stationary waves calculated for a deep, irrotational flow, $2\pi/k_0 = 2\pi U_0^2/g$. The semiaxes of the ellipses represent the uncertainty of the measurements reported by Horoshenkov et al. (2013).